IEEE Photonics Journal
An IEEE Photonics Society Publication

Open Access

Low Loss Hollow-Core Antiresonant Fiber With Nested Elliptical Cladding Elements

Volume 9, Number 1, February 2017

Fan-Chao Meng
Bo-Wen Liu
Yan-Feng Li
Ching-Yue Wang
Ming-Lie Hu

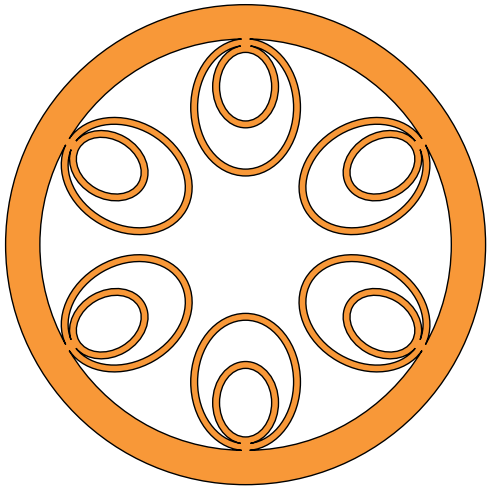

DOI: 10.1109/JPHOT.2016.2639044
1943-0655

IEEE photonics SOCIETY

IEEE

Low Loss Hollow-Core Antiresonant Fiber With Nested Elliptical Cladding Elements

Fan-Chao Meng, Bo-Wen Liu, Yan-Feng Li, Ching-Yue Wang, and Ming-Lie Hu

Ultrafast Laser Laboratory, Key Laboratory of Optoelectronic Information Science and Technology of Ministry of Education, College of Precision Instruments and Optoelectronics Engineering, Tianjin University, Tianjin 300072, China

DOI:10.1109/JPHOT.2016.2639044

Manuscript received November 11, 2016; revised December 7, 2016; accepted December 8, 2016. Date of publication December 13, 2016; date of current version December 30, 2016. This work was supported in part by the National Natural Science Foundation of China under Grant 61535009, Grant 61377047, and Grant 11274239 and in part by the Program for Changjiang Scholars and Innovative Research Team in University under Grant IRT13033. Corresponding author: M. Hu (e-mail: huminglie@tju.edu.cn).

Abstract: We design and investigate the optical properties of a novel hollow-core antiresonant fiber with nested elliptical cladding elements. This new structure shows low confinement loss even with a relatively small core. The lowest confinement loss of this structure is more than two orders of magnitude smaller than its circular-element counterparts. When the size of the cladding elements is properly designed, higher order core modes resonantly couple with the cladding modes effectively, resulting in an extremely high higher order-mode extinction ratio ($>10^4$). This good single mode performance can be achieved for a wide range of cladding element parameters, which would increase the fabrication tolerance. The new fiber also shows low bending loss for a wide range of bend radii. Moreover, dispersion properties of the new structure are also investigated under both unfilled and filled conditions. Numerical results show that antiresonant structures with the same core diameter and strut thickness have similar dispersion curves. The zero dispersion wavelength within the fundamental antiresonant transmission band can be tuned over tens of nanometers by increasing the pressure up to 50 bar when the fiber is filled with argon.

Index Terms: Waveguides, fiber optics systems, modeling.

1. Introduction

Dielectric hollow fibers have many unique features compared with their solid-core counterparts. Hollow fibers can usually sustain high laser power and show low dispersion and nonlinearity. When filled with gases, the guidance properties of hollow fibers can be easily tuned by changing the gas species or by adjusting the gas pressure [1]. The simple capillary has been an important tool for pulse compression [2], deep-ultraviolet ultrashort pulse generation [3] and high-harmonic generation [4]. However, the relatively high loss has limited the performance of the capillary. It has to be made with a relatively large diameter to achieve a reasonable loss, resulting in only normal dispersion at usable pressure levels [5].

Microstructure hollow fibers significantly reduce the loss. The optical properties can be easily tailored via changing the cladding structures. One type of microstructure hollow fiber is the hollow-core photonic bandgap (HC-PBG) fiber. It guides light by the out-of-plane photonic bandgap formed by periodic arrangement of air holes in a silica background [6]. The HC-PBG fiber offers a minimum

attenuation loss of only 1.2 dB/km at telecommunication wavelengths [7]. However, the bandwidth of the PBG fiber is usually only 30% of the central wavelength [8]. Another successful hollow fiber is the Kagome fiber. The guiding mechanism of Kagome fiber is different from that of HC-PBG fiber, being inhibited coupling between the core mode and cladding modes [9]. The bandwidth of Kagome fiber can be very wide and reach several hundred nanometers [5]. In 2011, a hypocycloid-core Kagome fiber was proposed with lower attenuation than the regular Kagome fiber [10], which motivates later intensive studies on the negative curvature hollow-core fiber (NC-HCF), also called hollow-core anti-resonant fiber (HC-ARF) [11]. Other types of microstructure hollow fibers such as tube-lattice hollow-core fibers have also been proposed for terahertz wave transmission [12]–[14].

A variety of negative-curvature hollow-core fibers have been investigated. Pryamikov *et al.* proposed the first NC-HCF for 3 μm transmission in 2011, and the fiber consisted of only one row of eight touched capillaries in the cladding [15]. Later it was demonstrated by Kolyadin *et al.* that the confinement loss can be reduced if capillaries in the cladding are designed to non-touching [16]. In 2014, Berladi *et al.* proposed a novel structure by adding extra tubes within the air cladding region of the NC-HCF [17]. The loss of this new structure is significantly lower than that of the previous NC-HCF. Later, Poletti further proposed the nested anti-resonant nodeless fiber (NANF). It was numerically shown that in principle the NANF can reach a total value of loss lower than that of conventional solid core fibers [8]. Moreover, it was also shown in [8] that fibers with only six nested cladding elements can improve the performance. The NANFs have been fabricated for low loss operation both with different [18] and the same [19] wall thickness between the inner and outer cladding tubes. HC-ANF with large birefringence were also proposed recently [20]. A more detailed description of the historical development of NC-HCFs can be found in [11]. Most anti-resonant fibers that have been proposed are based on circular anti-resonant elements in the cladding. A new type of anti-resonant fiber based on a single layer of elliptical anti-resonant elements has been proposed recently [21]. The new structure has the advantages of lower confinement loss, better single mode operation and improved bending loss compared with the single layer circular-element structure.

In this paper, we intend to study the elliptical-element-based anti-resonant fiber further by adding extra elliptical tubes to the cladding. This elliptical-element nested anti-resonant nodeless fiber (ENANF) shows much lower confinement loss than both circular-element nested structures [17] and single row elliptical-element structures [21] of the same core size. We design and investigate the optical properties of the ENANF with a relatively small size, which is favored in many applications such as ultrashort pulse compression and nonlinear frequency conversion in fibers [1]. The laser intensity will be greatly enhanced if the diameter of the core can be decreased. Therefore, a structure that both has a relatively small core size and can still maintain good loss performance is needed. For the circular-element ARFs, when the core diameter decreases, the size of the cladding tubes also decreases proportionally. Therefore, the distance between the core and jacket tubes decreases. As a result, the loss increases when the core diameter is reduced [8], [21]. This is one of the reasons why most ANFs with circular cladding elements that have been fabricated or studied numerically all have a core diameter much larger (more than 30-fold) than the working wavelength [8], [17], [22]–[24]. In contrast, for elliptical-element cladding structures, the minor and major axes can be designed separately. Therefore, they do not need to change proportionally and a large enough distance between the core and jacket can be kept even when the core is decreased. Moreover, because of the increased curvature, the elliptical-element anti-resonant fiber (EANF) can provide much lower loss than a circular-element structure of the same size. Therefore, the ENANF is a good candidate which can be made with a small core size and maintain good loss performance at the same time. We note that in [21] the major axis length of the cladding ellipses is fixed and only the minor axis length is changed for optimization. Here, we show that by changing the length of both axes of the cladding tubes the loss performance can be further optimized.

2. Structure and Simulation Results

The geometries of four different HC-ARFs are shown in Fig. 1, i.e., (a) anti-resonant nodeless fiber (ANF), (b) nested anti-resonant nodeless fiber (NANF), (c) elliptical-element anti-resonant nodeless

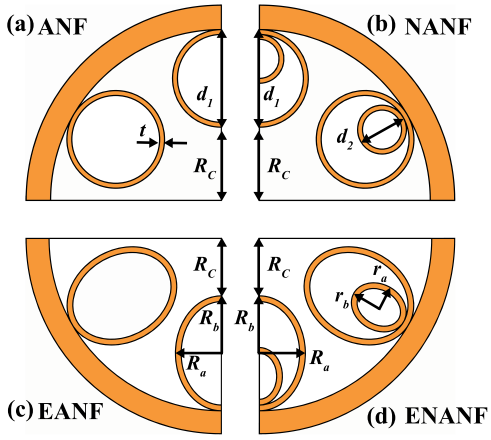

Fig. 1. Geometries of different HC-ARFs. All structures have the same core radius R_c and strut thickness t. (a) Anti-resonant nodeless fiber (ANF), where the diameter of the cladding tubes is d_1. (b) Nested anti-resonant nodeless fiber (NANF), where the diameters of outer cladding tubes and inner tubes are d_1 and d_2, respectively. (c) Elliptical-element anti-resonant nodeless fiber (EANF), where the semi-major and semi-minor axes of the cladding tubes are R_b and R_a, respectively. (d) Elliptical-element nested anti-resonant nodeless fiber (ENANF), where the semi-major and semi-minor axes of the outer cladding tubes are R_b and R_a, respectively, and the semi-major semi-minor axes of the inner cladding tubes are r_b and r_a, respectively.

fiber (EANF), and (d) elliptical-element nested anti-resonant nodeless fiber (ENANF). All structures have six elements in the azimuthal direction here, and only a quarter of the geometry is shown here for each structure. We have used similar terminology as in [8]. The first two structures have been studied by many authors, and the third structure was proposed recently [21]. The last structure has been reported by Chaudhuri *et al.* [25] recently. However, only confinement loss were investigated in [25] while more guidance properties such as single mode performance, bending loss and dispersion still need investigation. Furthermore, in [25] the size of the major axis of the outer ellipses were fixed to be equal to the size of the core and the size of minor axis of the outer ellipses were also fixed. Only the size of the inner ellipses were changed when optimize the loss performance. To fully optimize the guidance properties of the ENANF, the size of both the inner and outer ellipses need to be scanned. Here we assume that all structures have the same core diameter R_c and strut thickness t as shown in Fig. 1. Most reports have mainly focused on designing anti-resonant fibers working at 1 μm or in the mid-infrared. Here we design a structure working at 800 nm which is the output central wavelength of the commonly used Ti: Sapphire femtosecond laser. The fiber is intended to be used in nonlinear effects around this wavelength. We choose the strut thickness $t = 280$ nm which makes the first resonant region around $\lambda = 2t/\sqrt{n_{gl}^2 - 1} = 531$ nm. The core radius is set as $R_c = 10\lambda_0 = 8$ μm with $\lambda_0 = 800$ nm. Here the core radius is smaller than those reported in most theoretical studies [8], [17], [21], [26], [27]. A smaller core diameter have many advantages. As mentioned before, it is less sensitive to the bend loss and can result in higher laser intensity in nonlinear propagation. However, a smaller core size may cause higher confinement loss for anti-resonant fiber structures, which, however, can be reduced by proper design of the ENANF.

Four parameters (ξ_1, ξ_2, η_1, η_2) are defined to control the cladding size of the structures shown in Fig. 1. $\xi_1 = d_1/(2R_c)$ and $\xi_2 = d_2/d_1$ are applied for ANF and NANF structures. For ANF, d_1 is the diameter of the cladding tubes. For NANF, d_1 is the diameter of the outer cladding tubes and d_2 that of the inner ones. For EANF and ENANF, we call the axis in the radical direction the major axis and that in the azimuthal direction the minor axis for the cladding ellipses, and this terminology is appropriate for most of the useful low loss structure parameters, as will be shown in the following sections. Similarly, we define $\xi_1 = R_b/R_c$ and $\xi_2 = r_b/R_b$ for EANF and ENANF structures. For EANF, R_b is the length of the semi-major axis of the cladding tubes, and for ENANF, R_b is the length of the semi-major axis of the outer cladding tubes, and r_b is the length of the semi-major axis of the

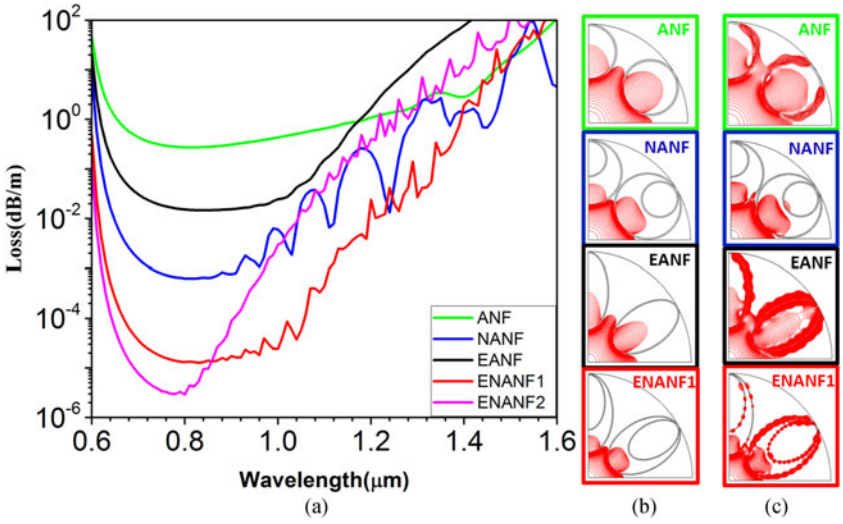

Fig. 2. Comparison of confinement loss between different structures. (a) Calculated loss spectra and (b) and (c) logarithmic scale contour plots of the z-Poynting vector of the fundamental mode at 800 nm and 1600 nm, respectively.

inner cladding tubes. More parameters should be defined to quantify the length of the semi-minor axis of the cladding ellipses. For EANF, there is a maximum semi-minor axis length when the length of the semi-major axis is chosen. The maximum semi-minor axis length can be represented as

$$R_{a,\max} = \tan(\theta/2)\sqrt{R_c^2 + 2R_bR_c} \tag{1}$$

where θ is the angle between two adjacent cladding elements in the azimuthal direction, and $\theta = \pi/3$ for structures investigated here. $R_{a,\max}$ defined by (1) is the length of the semi-minor axis when the cladding tubes are tangent to each other for EANF. We define $\eta_1 = R_a/R_{a,\max}$ to characterize the size of the semi-minor axis R_a. This definition is also used for the outer cladding ellipses of ENANF. Another parameter is needed to characterize the size of the semi-minor axis of the inner ellipses for ENANF. To avoid intersection with the outer ellipses, we let the radius of curvature in the major axis direction of the outer ellipses equal to that of the inner ellipses to obtain the maximum semi-minor axis of the inner ellipses $r_{a,\max}$

$$r_{a,\max} = R_a\sqrt{r_b/R_b}. \tag{2}$$

We define $\eta_2 = r_a/r_{a,\max}$ to characterize the length of the minor axis r_a of the inner ellipses. The commercial available full-vector finite element-based software package Comsol Multiphysics was applied to calculate the loss and modal indices for all structures. To accurately calculate the confinement loss, we utilized a perfectly matched layers (PML) boundary in the outmost of the geometries. The PML needs to be carefully optimized and extremely fine meshes need to be used to obtain accurate results [8]. We have validated our calculation by repeating the results in [8] and [17].

2.1 Confinement Loss

The loss spectra are shown in Fig. 2 for the four different structures. The material loss is neglected since the material absorption is quite low in this wavelength range [28]. Each structure was optimized individually to show relatively low loss at 800 nm. The first two structures both have circular cladding elements and have been intensively investigated [11], [26], [27], [29]. The EANF has been proposed by Habib *et al.* recently [21] and shown to have low confinement loss and good single mode behavior. The ENANF proposed here will be shown to have superior properties compared with the other three types.

TABLE 1
Parameters of Different Structures Optimized for Low Loss at 800 nm

Fiber type	ξ_1	ξ_2	η_1	η_2	Loss(dB/m) at 800 nm
ANF	0.66	–	–	–	2.73×10^{-1}
NANF	0.97	0.55	–	–	6.36×10^{-4}
EANF	1.25	–	0.70	–	1.53×10^{-2}
ENANF1	1.62	0.70	0.85	0.82	1.32×10^{-5}
ENANF2	1.47	0.75	0.80	0.74	3.99×10^{-6}

We scan the parameters ξ_1, ξ_2, η_1, and η_2 to fully optimize the structures at 800 nm. The optimized parameters corresponding to curves in Fig. 2(a) are listed in Table 1.

The ANF structure has the highest loss among all structures although it shows the most flat behavior as can be seen in Fig. 2(a). The loss of the EANF structure is lower than the ANF around 800 nm but increases rapidly at longer wavelengths due to strong coupling between the core mode and cladding modes. Habib *et al.* have clarified the advantages of the EANF in depth [21]. It should be noted that both the major- and minor-axis lengths of the ellipses are scanned simultaneously to obtain the optimum loss performance at 800 nm here. In [21], the major axis is kept a constant and only the length of the minor axis is scanned to optimize the loss. The NANF shows lower loss than the un-nested ANF and EANF structures due to contribution of the additional inner anti-resonant elements. For the ENANF, we have shown the loss curves for two sets of parameters; one with the lowest loss at 800 nm is represented by the magenta line in Fig. 2(a), while the other represented by the red line gives a wider low loss band. The loss curves of the ENANF also shows some oscillations because of the coupling effect, which seems to be inherent for nested structures. Fig. 2(b) shows in logarithmic scale the contour plots of the normalized z-Poynting vector of fundamental mode for those four structures at 800 nm, the value ranging from -60 to 0 dB. It can be seen that the nested structures confine the field better than their un-nested counterparts. The reason about why the nested structure has lower leakage loss may be understood from the following. Although (E)ANFs with single layer of anti-resonant elements confine most of the field inside the core, there is still a small amount of field penetrating into the cladding tubes and even further into the jacket which would increase the confinement loss. This can be seen from the contour plots of z-Poynting vector shown in Fig. 2(b). When additional anti-resonant elements are added into the cladding tubes, they also work in anti-resonance and can reflect the penetrating field to the core by Fresnel reflection. As a result, more field are confined inside the core and the leakage or confinement loss is decreased. The loss increases rapidly at longer wavelengths for all structures because of the increased coupling between the core mode and cladding ring modes. Fig. 2(c) gives the corresponding plots at 1600 nm. There is obviously more field localized in the cladding tubes at 1600 nm than at 800 nm. The coupling is significantly intense for the EANF structure. This fact will later be seen from Fig. 3(a) because of the little difference in the effective index between the core mode and the ring modes of the elliptical tubes in the cladding, which yields better phase matching between these two modes.

Due to the good confinement performance, the leakage loss of ENANF shown here is in the scale of 10^{-4} dB/m and even lower. It should be noted that surface scattering loss, which becomes the dominant source of loss in ultra-low loss HC-PBGFs [7], may play a role in the overall loss performance [8].

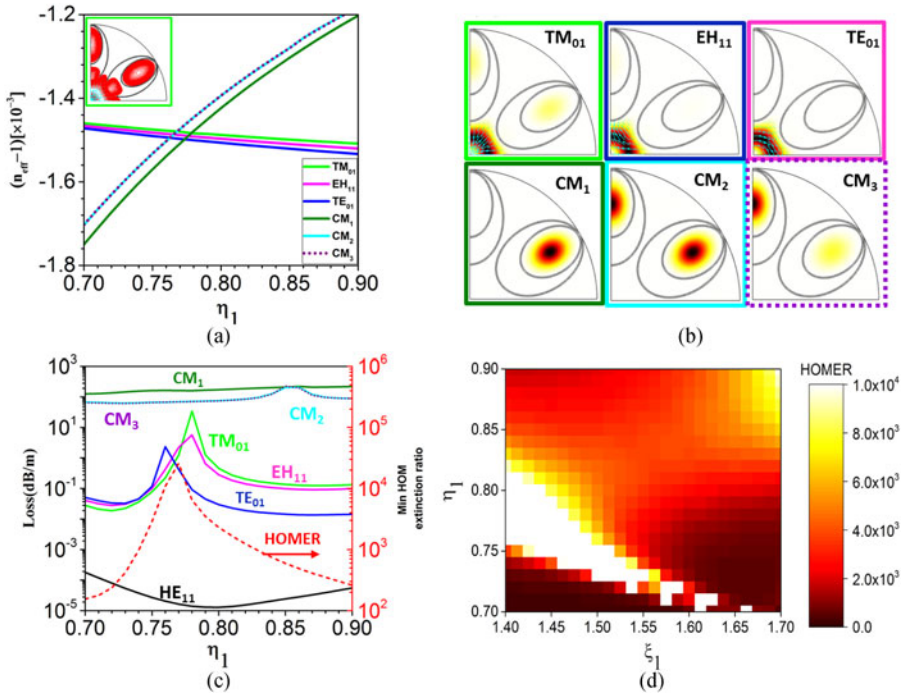

Fig. 3. Single mode performance of ENANF at 800 nm. (a) Mode index curves and (c) loss curves and minimum higher-order mode extinction ratio (HOMER) as a function of η_1 at $\xi_1 = 1.4$ for some higher order core modes and cladding modes. The inset in the top left of (a) shows the contour plot of z-Poynting vector of TM_{01} mode in logarithmic scale at $\eta_1 = 0.78$. (b) Density plots of z-Poynting vector for different modes. (d) Density plot of HOMER for TM_{01} mode as functions of η_1 and ξ_1.

2.2 Single Mode Performance

Anti-resonant fibers are leaky fibers and always sustain a multitude of air modes. This is similar with that of Bragg fibers which support an infinite number of leaky modes [30]. In this section, we investigate the single mode property of the ENANF. We have calculated the loss of the first four lowest order modes: HE_{11}, TM_{01}, TE_{01}, and EH_{11} mode. When the loss of the higher-order modes are significantly higher than that of the fundamental mode, the fiber will perform effectively as a single mode fiber. This can be achieved by changing the parameters of the cladding tubes. We have defined four parameters above for controlling the fiber geometries. For simplicity, we scan the length of the two semi-axes of the outer ellipses independently while keeping the two semi-axes of the inner ellipses proportionally. The parameter ξ_1 representing the length of the semi-major axis ranges from 1.4 to 1.7, and η_1 for the semi-minor axis ranges from 0.7 to 0.9. We keep $\xi_2 = 0.7$ and $\eta_2 = 0.82$ during the scanning, and therefore, the inner ellipse changes proportionally with the outer ellipse.

Fig. 3(a) plots the effective index (n_{eff}-1) as a function of η_1 with $\xi_1 = 1.4$ at 800 nm for different modes and Fig. 3(b) shows the typical mode patterns for these modes. We term the three cladding modes CM_i, ($i = 1, 2, 3$). The effective mode indices of the three higher-order core modes (TM_{01}, EH_{11}, and TE_{01}) decrease monotonically with η_1, while those of the three cladding modes (CM_1, CM_2, and CM_3) increase monotonically with η_1. This originates from the decrease of the effective area of the core and the increase of the effective area of the cladding ellipses when η_1 varies from 0.7 to 0.9. The index curves of the three higher-order core modes intersect with those of the cladding modes around $\eta_1 = 0.76$ and 0.78, which results in high loss for the higher-order core modes. The inset in Fig. 3(a) shows the contour plot of the z-Poynting vector of TM_{01} mode in logarithmic scale at $\eta_1 = 0.78$. It serves as an example of the mode coupling effect, where the TM_{01} mode couples strongly with the cladding mode, resulting in a significantly high loss. Fig. 3(c) displays the confinement loss for the core and cladding modes. The dark solid curve corresponding to loss of

the fundamental HE_{11}-like mode reaches a minimum around $\eta_1 = 0.8$ and is not influenced by the cladding modes. The loss curves of three higher order core modes (TM_{01}, EH_{11}, and TE_{01}) reach a maximum around $\eta_1 = 0.76$ and 0.78, which correspond to the crossing points between the higher-order core modes and cladding modes in Fig. 3(a). The cladding modes CM_2 and CM_3 are nearly degenerate, as can be seen from the nearly identical loss curves and the index curves, where the CM_3 mode is represented by the dotted curve to distinguish from the CM_2 mode. We also use the higher-order mode extinction ratio (HOMER) to quantitatively describe the single mode performance [8], [23], [29]. HOMER is defined as the ratio of the loss of the higher-order core modes to that of the fundamental mode. The red dashed curve in Fig. 3(c) represents the minimum HOMER, where the highest value can reach more than 10^4 around $\eta_1 = 0.77$ and is more than 10^3 when η_1 ranges from 0.74 to 0.82, which means a good fabrication tolerance for single mode design.

Fig. 3(d) shows the density plot of HOMER for TM_{01} mode when both ξ_1 and η_1 corresponding to the semi-major and semi-minor axes, respectively, are changing. When ξ_1 increases from 1.4 to 1.7, the maximum HOMER point (corresponding to the phase matching point) for η_1 decreases. This can be understood from change in the effective mode index of different modes. The cladding mode index changes more rapidly with the cladding tubes than the core mode index as shown in Fig. 3(a). Therefore, when the semi-major axis of the cladding ellipses is enlarged, the semi-minor axis needs to be reduced to ensure that the index of the cladding modes is still equal to that of the higher-order core mode. It can be seen from Fig. 3(d) that for most parameters the HOMER is above 10^3, which means excellent single mode performance. We have only scanned two parameters ξ_1 and η_1 while keeping ξ_2 and η_2 constant, and hence, if all the four parameters are scanned simultaneously, there will be a larger parameter space for excellent single mode operation. The fabrication tolerance for single mode operation will also benefit from this.

2.3 Bending Loss

Bending loss is an important factor for fiber applications. It has been demonstrated that an additional ring of elements can help to improve the bend robustness [8]. Moreover, the bending loss may also benefit from the relatively small core size [11], [31]. Therefore, the ENANF structure is expected to show good performance in bending loss. We use the conformal transformation method [32] to transform the refractive index of the bended fiber into an equivalent straight fiber:

$$n'(x, y) = n(x, y) \exp(x/R_{bend}) \tag{3}$$

where $n'(x, y)$ is the conformed index distribution, $n(x, y)$ is the index distribution before bending, and R_{bend} is the bend radius.

We have assumed that the bending direction is along the x-axis. Fig. 4(a) shows the bending loss curves of the fundamental modes of the NANF, EANF, and ENANF both for the x-polarized and y-polarized electric field which are represented by the dash doted and solid lines respectively. The ANF is not considered here since it has much higher loss than the other structures. The structure parameters of the NANF and EANF are the same as those listed in Table 1, and we choose $\xi_1 = 1.45$ for the ENANF which gives a lower loss at 800 nm. It can be seen that when the bend radius is above 5 cm, the bending loss decreases monotonically with the bend radius for all structures. The ENANF shows the lowest bending loss for a wide range of band radii despite at which induce coupling between the core mode and cladding mode. The mode pattern at the top of Fig. 4(b) shows the normalized intensity of the z-Poynting vector for $R_{bend} = 1$ cm corresponding to the solid blue square in Fig. 4(a), where it can be seen that the field distribution has a displacement due to bending. The loss peak in the loss curve of the ENANF in Fig. 4(a) around $R_{bend} = 3.5$ cm (marked by the red solid square) originates from the phase matching between the core mode and cladding mode after bending. The mode pattern at the bottom of Fig. 4(b) shows the z-Poynting vector plot in logarithmic scale to show the coupling more clearly. Similar effects also happen for the EANF with corresponding peaks in Fig. 4(a). The bending loss peaks due to the coupling effect are sensitive to the structure parameters. Fig. 4(c) shows the bending loss of the y-polarized electric fields of fundamental mode for different structure parameters ξ_1, while the other parameters are

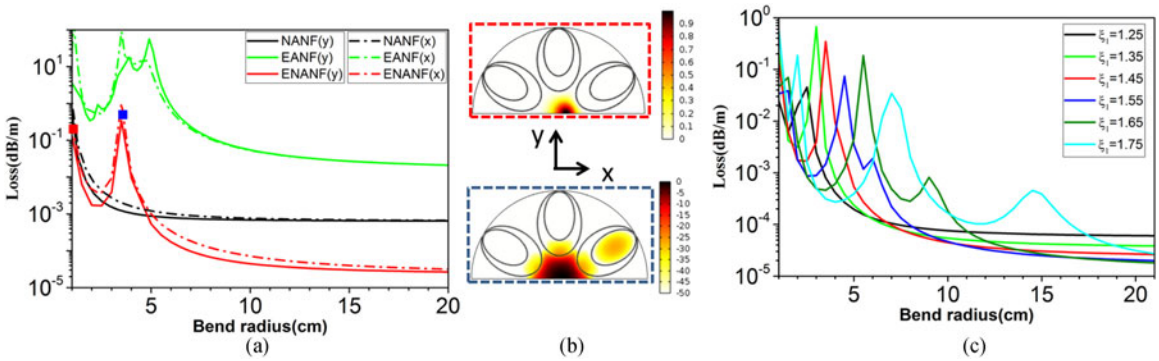

Fig. 4. Calculated bending loss at 800 nm. (a) Bending loss curves versus bending radius for x- and y-polarized electric fields of fundamental mode of NANF, EANF, and ENANF, where the red and blue squares on the solid ENANF curve correspond to the intensity distributions at the top and bottom of Fig. 4(b), respectively. (b) Top: normalized intensity of z-Poynting vector at $R_{bend} = 1$ cm for ENANF; bottom: intensity plot of z-Poynting vector in logarithmic scale at $R_{bend} = 3.5$ cm for ENANF. (c) Bending loss curves versus bending radius for different sizes of semi-major axis of the outer cladding ellipses.

unchanged. It can be seen that when the semi-major axis increases, the peak shifts to a larger bend radius. Therefore, there is a trade-off between the transmission bandwidth and the bending loss performance, because a wider transmission bandwidth requires a longer semi-major axis as shown in Fig. 1(a) but a better bending loss performance will need a shorter one.

2.4 Dispersion Properties

The dispersion property is very important for many applications such as pulse compression and nonlinear frequency conversion [5]. In this section, we investigate the dispersion property of the ENANF in both filled and un-filled regimes. Fig. 5(a) shows the second-order dispersion for different structures. The geometry parameters of these structures are the same as those in Table 1. For the ENANF we use the parameters of ENANF1 in Table 1, which gives a wider transmission bandwidth. It can be observed that the dispersion curves are quite similar for all structures despite the fact that the losses are quite different as shown in Fig. 2. The dispersion values are quite low and are on the order of tens of fs^2/cm, which are significantly lower than that of a solid fiber or HC-PBGF [5], [11]. This feature makes the anti-resonant fibers suitable for high intense ultrashort laser pulse transmission.

In Fig. 5(a) we also show the dispersion curve of a hollow dielectric waveguide [31] with the same core diameter as that of the other structures. The dispersion of the hollow dielectric waveguide is calculated from the propagation constant formula of the capillary model (CM) derived by Marcatili and Schmeltzer [31]:

$$\beta = \frac{2\pi}{\lambda}\sqrt{n^2 - (u_{11}/k_0 R_c)^2} \tag{4}$$

where β is the propagation constant, λ is the transmission wavelength, n is the refractive index of the filling material, u_{11} is the first root of the zero-order Bessel function, k_0 is the propagation constant in vacuum, and R_c is the core radius. Without any filled gas, the dispersion of the capillary model is anomalous for all wavelengths [1], [5], and this is significantly different from that of anti-resonant fibers. Within the transmission band the sign of dispersion for anti-resonant fibers changes from positive to negative as the wavelength increases. The dispersion curve has a zero point around $\lambda = 700$ nm which is at the shorter wavelength side of the transmission window [11]. Since in most applications the fiber is filled with gases at different pressures to allow for tunability. Here, we also investigate how the dispersion curve changes with the filling gas pressure. Without loss of generality, we assume that the fibers are filled with argon. The dispersion and loss of the ENANF are calculated for different pressures ranging from 2 bar to 50 bar. The dispersion formula is extracted from [33].

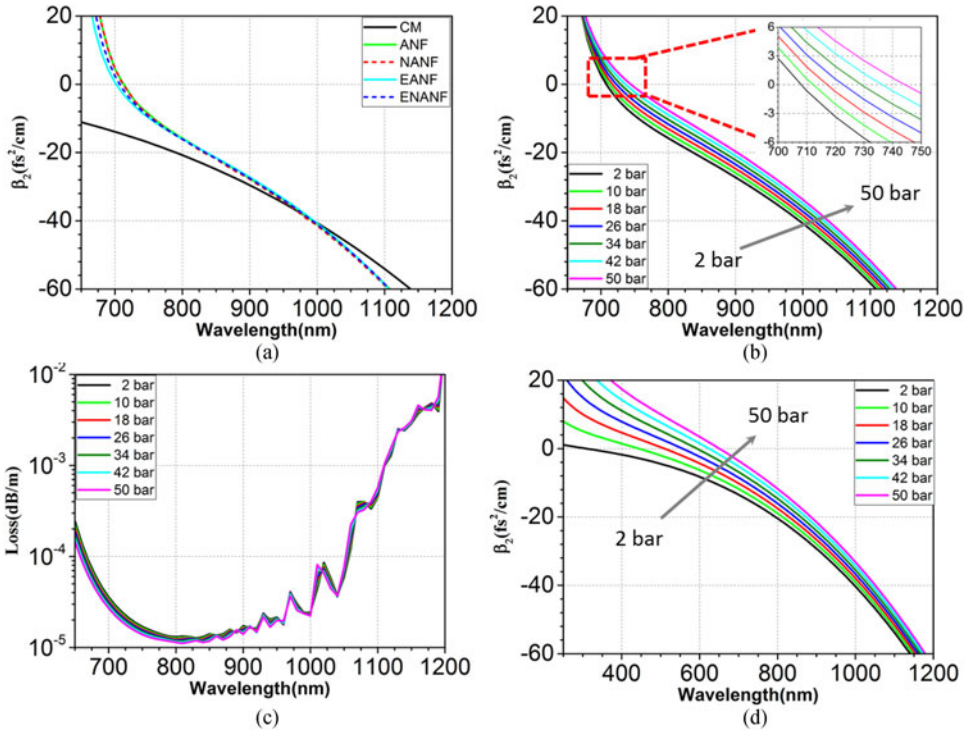

Fig. 5. Calculated second-order dispersion for different structures. (a) Dispersion curves for different structures listed in Table 1 and the capillary model (CM) [31]. (b) Dispersion and (c) confinement loss of ENANF when filled with argon at different pressures ranging from 2 bar to 50 bar. (d) Dispersion calculated from the capillary model when filled with argon at different pressures ranging from 2 bar to 50 bar.

Fig. 5(b) shows the dispersion curves at different filling pressures, where the zero dispersion wavelength (ZDW) shifts to longer wavelengths as the filling pressure is increased. The inset above shows a close-up view of the dispersion near the ZDW. It can be seen that by changing the filling pressure the ZDW can be tuned over 40 nm. Fig. 5(c) shows the corresponding losses which are nearly unchanged at different filling pressures. The dispersion of the hollow dielectric waveguide at different pressures is calculated and shown in Fig. 5(d), where the ZDW also shifts to longer wavelengths when the pressure is increased. However, the ZDW shifts further than ANFs due to the weak anomalous dispersion within the whole spectrum when not filled.

3. Conclusion

We have proposed a novel anti-resonant fiber with nested elliptical anti-resoant elements in the cladding. Because of its excellent performance in confinement loss, the structure can be designed with a relatively small core diameter which would increase the intensity of guided laser for nonlinear applications. Although we mainly focus on the performance around 800 nm, the output wavelength of Ti: Sapphire lasers, our results can be extended to other wavelengths by scaling. The confinement loss is significantly lower than its circular-element counterparts. Moreover, there are more freedoms for designing the elliptical-element structure since both the semi-major and minor axis sizes can be changed simultaneously. The ENANF shows an excellent single mode performance when the parameters are properly chosen such that the higher-order core modes are phase matched to cladding modes while the fundamental core mode is not affected. An HOMER of more than 10^4 can be achieved for a wide range of parameters. The bending loss of the ENANF is strongly influenced by structure parameters. Structures with a shorter semi-major axis have better bending loss performance. Therefore, there is a trade-off between the transmission bandwidth and the

bending loss performance. The dispersion of the ENANF is quite different from that of the hollow dielectric waveguide. The dispersion switches it sign from positive to negative within the transmission band while the hollow dielectric waveguide shows anomalous dispersion for all wavelengths when not filled. With an increase of the pressure of the filling gas, the ZDW shifts to longer wavelengths. The ZDW change is larger for the hollow dielectric waveguide than for the ENANF.

If the inner and outer elements in the cladding have a different thickness, the loss spectra will be affected since different thicknesses correspond to different resonant wavelengths and transmission bands. NANFs with different inner and outer circular anti-resonant elements in the cladding have been designed to broaden the transmission bandwidth [18]. It is reasonable to expect that the transmission bandwidth of ENANFs may also be broadened if different inner and outer elements are used and properly designed.

In a future work we will investigate how the number of nested elements in the azimuthal direction affects the loss performance. For NANFs with circular elements more cladding elements result in a shorter distance between the core and the jacket tube, which will increase the loss. This is no longer true for NANFs with elliptical elements since the semi-major and minor axes can be designed separately. Therefore, we expect that more than six cladding tubes may also perform well in terms of both the confinement loss and bending loss.

Acknowledgment

The authors would like to thank Prof. L. Vincetti of University of Modena and Reggio Emilia, Italy; Dr. W. Belardi of University of Southampton, U.K.; and Dr. M. Habib of Technical University of Denmark for the useful discussions.

References

[1] P. S. J. Russell, P. Hölzer, W. Chang, A. Abdolvand, and J. Travers, "Hollow-core photonic crystal fibres for gas-based nonlinear optics," *Nature Photon.*, vol. 8, no. 4, pp. 278–286, 2014.
[2] M. Nisoli, S. De Silvestri, and O. Svelto, "Generation of high energy 10 fs pulses by a new pulse compression technique," *Appl. Phys. Lett.*, vol. 68, no. 20, pp. 2793–2795, 1996.
[3] C. G. Durfee, S. Backus, H. C. Kapteyn, and M. M. Murnane, "Intense 8-fs pulse generation in the deep ultraviolet," *Opt. Lett.*, vol. 24, no. 10, pp. 697–699, 1999.
[4] T. Popmintchev, M.-C. Chen, P. Arpin, M. M. Murnane, and H. C. Kapteyn, "The attosecond nonlinear optics of bright coherent x-ray generation," *Nature Photon.*, vol. 4, no. 12, pp. 822–832, 2010.
[5] J. C. Travers, W. Chang, J. Nold, N. Y. Joly, and P. S. J. Russell, "Ultrafast nonlinear optics in gas-filled hollow-core photonic crystal fibers [invited]," *J. Opt. Soc. Amer. B*, vol. 28, no. 12, pp. A11–A26, 2011.
[6] F. Benabid and P. Roberts, "Linear and nonlinear optical properties of hollow core photonic crystal fiber," *J. Mod. Opt.*, vol. 58, no. 2, pp. 87–124, 2011.
[7] P. Roberts *et al.*, "Ultimate low loss of hollow-core photonic crystal fibres," *Opt. Exp.*, vol. 13, no. 1, pp. 236–244, 2005.
[8] F. Poletti, "Nested antiresonant nodeless hollow core fiber," *Opt. Exp.*, vol. 22, no. 20, pp. 23807–23828, 2014.
[9] F. Couny, F. Benabid, P. Roberts, P. Light, and M. Raymer, "Generation and photonic guidance of multi-octave optical-frequency combs," *Science*, vol. 318, no. 5853, pp. 1118–1121, 2007.
[10] Y. Wang, N. V. Wheeler, F. Couny, P. Roberts, and F. Benabid, "Low loss broadband transmission in hypocycloid-core kagome hollow-core photonic crystal fiber," *Opt. Lett.*, vol. 36, no. 5, pp. 669–671, 2011.
[11] F. Yu and J. Knight, "Negative curvature hollow core optical fiber," *IEEE J. Sel. Topics Quantum Electron.*, vol. 22, no. 2, pp. 1–11, 2016.
[12] J.-Y. Lu *et al.*, "Terahertz air-core microstructure fiber," *Appl. Phys. Lett.*, vol. 92, no. 6, 2008, Art. no. 064105.
[13] L. Vincetti and V. Setti, "Waveguiding mechanism in tube lattice fibers," *Opt. Exp.*, vol. 18, no. 22, pp. 23133–23146, 2010.
[14] L. Vincetti, "Single-mode propagation in triangular tube lattice hollow-core terahertz fibers," *Opt. Commun.*, vol. 283, no. 6, pp. 979–984, 2010.
[15] A. D. Pryamikov, A. S. Biriukov, A. F. Kosolapov, V. G. Plotnichenko, S. L. Semjonov, and E. M. Dianov, "Demonstration of a waveguide regime for a silica hollow-core microstructured optical fiber with a negative curvature of the core boundary in the spectral region$> 3.5\mu$m," *Opt. Exp.*, vol. 19, no. 2, pp. 1441–1448, 2011.
[16] A. N. Kolyadin, A. F. Kosolapov, A. D. Pryamikov, A. S. Biriukov, V. G. Plotnichenko, and E. M. Dianov, "Light transmission in negative curvature hollow core fiber in extremely high material loss region," *Opt. Exp.*, vol. 21, no. 8, pp. 9514–9519, 2013.
[17] W. Belardi and J. C. Knight, "Hollow antiresonant fibers with reduced attenuation," *Opt. Lett.*, vol. 39, no. 7, pp. 1853–1856, 2014.
[18] W. Belardi, "Design and properties of hollow antiresonant fibers for the visible and near infrared spectral range," *J. Lightw. Technol.*, vol. 33, no. 21, pp. 4497–4503, Nov. 2015.

[19] A. F. Kosolapov *et al.*, "Hollow-core revolver fibre with a double-capillary reflective cladding," *Quantum Electron.*, vol. 46, no. 3, pp. 267–270, 2016.
[20] W. Ding and Y.-Y. Wang, "Hybrid transmission bands and large birefringence in hollow-core anti-resonant fibers," *Opt. Exp.*, vol. 23, no. 16, pp. 21165–21174, 2015.
[21] M. S. Habib, O. Bang, and M. Bache, "Low-loss single-mode hollow-core fiber with anisotropic anti-resonant elements," *Opt. Exp.*, vol. 24, no. 8, pp. 8429–8436, 2016.
[22] F. Yu, W. J. Wadsworth, and J. C. Knight, "Low loss silica hollow core fibers for 3–4 μm spectral region," *Opt. Exp.*, vol. 20, no. 10, pp. 11153–11158, 2012.
[23] M. S. Habib, O. Bang, and M. Bache, "Low-loss hollow-core silica fibers with adjacent nested anti-resonant tubes," *Opt. Exp.*, vol. 23, no. 13, pp. 17394–17406, 2015.
[24] C. Wei, C. R. Menyuk, and J. Hu, "Impact of cladding tubes in chalcogenide negative curvature fibers," *IEEE Photon. J.*, vol. 8, no. 3, Jun. 2016, Art. no. 2200509.
[25] S. Chaudhuri, L. D. Van Putten, F. Poletti, and P. J. Sazio, "Low loss transmission in negative curvature optical fibers with elliptical capillary tubes," *J. Lightw. Technol.*, vol. 34, no. 18, pp. 4228–4231, Sep. 2016.
[26] M. S. Habib, O. Bang, and M. Bache, "Low-loss hollow-core anti-resonant fibers with semi-circular nested tubes," *IEEE J. Sel. Topics Quantum Electron.*, vol. 22, no. 2, pp. 156–161, Mar./Apr. 2016.
[27] A. Hartung *et al.*, "Low-loss single-mode guidance in large-core antiresonant hollow-core fibers," *Opt. Lett.*, vol. 40, no. 14, pp. 3432–3435, 2015.
[28] R. Kitamura, L. Pilon, and M. Jonasz, "Optical constants of silica glass from extreme ultraviolet to far infrared at near room temperature," *Appl. Opt.*, vol. 46, no. 33, pp. 8118–8133, 2007.
[29] C. Wei, R. A. Kuis, F. Chenard, C. R. Menyuk, and J. Hu, "Higher-order mode suppression in chalcogenide negative curvature fibers," *Opt. Exp.*, vol. 23, no. 12, pp. 15824–15832, 2015.
[30] C. M. de Sterke, I. Bassett, and A. G. Street, "Differential losses in bragg fibers," *J. Appl. Phys.*, vol. 76, no. 2, pp. 680–688, 1994.
[31] E. Marcatili and R. Schmeltzer, "Hollow metallic and dielectric waveguides for long distance optical transmission and lasers," *Bell Syst. Tech. J.*, vol. 43, no. 4, pp. 1783–1809, 1964.
[32] M. Heiblum and J. H. Harris, "Analysis of curved optical waveguides by conformal transformation," *IEEE J. Quantum Electronics*, vol. 11, no. 2, pp. 75–83, Feb. 1975.
[33] A. Börzsönyi, Z. Heiner, M. P. Kalashnikov, A. P. Kovács, and K. Osvay, "Dispersion measurement of inert gases and gas mixtures at 800 nm," *Appl. Opt.*, vol. 47, no. 27, pp. 4856–4863, 2008.